

Transition from positive to negative indirect CO₂ effects on the vegetation carbon uptake

Received: 22 July 2023

Accepted: 8 February 2024

Published online: 19 February 2024

 Check for updatesZefeng Chen ^{1,2,3}, Weiguang Wang ^{1,2,3} ✉, Giovanni Forzieri⁴ & Alessandro Cescatti⁵

Although elevated atmospheric CO₂ concentration (eCO₂) has substantial indirect effects on vegetation carbon uptake via associated climate change, their dynamics remain unclear. Here we investigate how the impacts of eCO₂-driven climate change on growing-season gross primary production have changed globally during 1982–2014, using satellite observations and Earth system models, and evaluate their evolution until the year 2100. We show that the initial positive effect of eCO₂-induced climate change on vegetation carbon uptake has declined recently, shifting to negative in the early 21st century. Such emerging pattern appears prominent in high latitudes and occurs in combination with a decrease of direct CO₂ physiological effect, ultimately resulting in a sharp reduction of the current growth benefits induced by climate warming and CO₂ fertilization. Such weakening of the indirect CO₂ effect can be partially attributed to the widespread land drying, and it is expected to be further exacerbated under global warming.

Terrestrial ecosystems absorb ~30% of anthropogenic carbon dioxide (CO₂) emissions and thus play a fundamental role in mitigating climate change^{1,2}. Over the past five decades, the terrestrial carbon sink has more than doubled at a pace that is consistent with the increase in anthropogenic CO₂ emissions^{2,3}. Current evidence demonstrates that the enhancement of the terrestrial carbon sink is partially attributable to the increased carbon uptake by vegetation under elevated atmospheric CO₂ concentration (eCO₂)^{4–7}. The eCO₂-induced changes in vegetation carbon uptake (represented by gross primary production (GPP)) are governed by two different mechanisms. The first is the direct effect of eCO₂ through the stimulation of photosynthetic carbon fixation and the enhancement of water-use efficiency (hereafter eCO₂(dir))^{8,9}. The second is the indirect effect of eCO₂ through its radiative forcing and the associated change in climate (e.g., temperature and water regime) and related environmental conditions (e.g., variation in nitrogen availability linked to temperature-driven changes in the mineralization rate of soil organic matter) (hereafter eCO₂(ind))^{10–12}. Recently, data-driven assessments based on in-situ and satellite observations have documented a declining trend in eCO₂(dir)^{9,13}. Given the dominant role of eCO₂ in the recent increase in

GPP¹⁴, the sign and temporal variation in eCO₂(ind) is expected to increasingly control the future trajectory of the terrestrial carbon budget¹⁵. However, the dynamics of such indirect CO₂ effect on the terrestrial carbon budget remain largely elusive. The relative importance of future indirect versus direct effects of eCO₂ in regulating vegetation carbon uptake has not yet been quantified, and the underlying ecological mechanisms remain poorly understood. Such knowledge gaps are reflected in substantial uncertainties in the effectiveness of land-based climate mitigation policies.

eCO₂(ind) originates from the strong and non-linear effects of eCO₂-induced climate change on terrestrial GPP, which involve multiple pathways, including the plants' response to changing temperature, water supply, atmospheric dryness (expressed by vapor pressure deficit, VPD) and their complex interactions¹⁶. In addition, these pathways via which climate influences GPP also interact with the eCO₂(dir)^{17,18}. For example, the rising VPD with eCO₂ generally causes a reduction in stomatal aperture, modulating the transpiration rate and—at the same time—the positive effect of CO₂ fertilization on photosynthesis¹⁹. In view of the variety of interacting feedbacks that regulate vegetation carbon uptake, it is challenging to quantitatively

¹National Key Laboratory of Water Disaster Prevention, Hohai University, Nanjing, China. ²Yangtze Institute for Conservation and Development, Hohai University, Nanjing, China. ³College of Hydrology and Water Resources, Hohai University, Nanjing, China. ⁴Department of Civil and Environmental Engineering, University of Florence, Florence, Italy. ⁵European Commission, Joint Research Centre, Ispra, Italy. ✉e-mail: wangweiguang@hhu.edu.cn

disentangle the total $eCO_2(\text{ind})$, particularly at regional-to-global scales, where local-scale findings of Free-air CO_2 enrichment (FACE) experiments may not be applicable^{20,21}. Recent studies based on satellite products and model simulations have reported the weakening of the temperature-vegetation relationship in northern ecosystems over the past 30 years²², the increasingly negative impact of VPD on alpine grassland productivity²³, and the increasing water constraint on vegetation growth in many regions across the globe^{24,25} and the corresponding higher risk of droughts to the global carbon cycle²⁶. However, considering that changes in temperature, atmospheric dryness, precipitation, and soil moisture are single components of the climate response to the CO_2 radiative forcing, findings of the above-mentioned studies can only partially reflect the temporal variations in $eCO_2(\text{ind})$. eCO_2 drives changes in various climatic factors, and their effects on vegetation carbon uptake are covariant, can be additive or offsetting, and may lead to nonlinearities due to different feedback mechanisms^{27,28}. Existing studies focusing on a single climate driver (e.g., temperature²²), generally assumed that the effects are independent by neglecting the covariation and the interaction between drivers. Therefore, the assessment of the variations in the total indirect effect of eCO_2 can only be partially represented.

To address these knowledge gaps, here we investigate the dynamics in $eCO_2(\text{ind})$ at the global scale for the period 1982–2014 using both satellite retrievals and an ensemble of Earth system models (ESMs) participating in the Coupled Model Intercomparison Project Phase 6 (CMIP6)²⁹ (Table 1), and project potential changes in $eCO_2(\text{ind})$ up to the year 2100 under the SSP5-8.5 scenario. Factorial simulations derived from the fully coupled experiment and the biogeochemically coupled experiment are used to disentangle the $eCO_2(\text{ind})$ signal for the historical and scenario periods³⁰ (Table 2, details in Methods). To further evaluate the robustness of model-based results, we retrieve the $eCO_2(\text{ind})$ term from satellite observations (hereafter $eCO_2(\text{ind})_{\text{obs}}$) through a statistical methodology within the climate analog framework (Methods). We complement the analyses by deriving $eCO_2(\text{dir})$ through multiple non-linear regression, incorporating CO_2 and climate drivers, and exploring its relationship with $eCO_2(\text{ind})$ across time and space. Finally, we investigate the sensitivity of $eCO_2(\text{ind})$ on land aridity to elucidate the underlying eco-hydrological mechanisms.

Results

Temporal change in the indirect effect of eCO_2

An ensemble of historical simulations from seven CMIP6 models (CMIP6_{SMA}, SMA: simple model averaging) shows that global $eCO_2(\text{ind})$ during the period 2000–2014 is significantly ($p < 0.05$, t test) lower than that during 1982–1996 (Fig. 1a, b). Averaged across the global vegetated areas, $eCO_2(\text{ind})$ simulated by CMIP6 models decreases from $0.24 \pm 0.32 \text{ gC m}^{-2} \text{ ppm}^{-1}$ (mean \pm s.e.) during 1982–1996 to $-0.04 \pm 0.24 \text{ gC m}^{-2} \text{ ppm}^{-1}$ during 2000–2014 (Fig. 1a, b). The emergence of negative $eCO_2(\text{ind})$ during 2000–2014 suggests the recent upsurge of climate stresses on the global vegetation carbon uptake, which is in agreement with the negative contribution of climate change on global GPP trend after 2000s reported in previous literature³¹.

Remarkable differences in changes in $eCO_2(\text{ind})$ emerge across geographic areas and climatological gradients. Cold and dry climate zones experience a prominent decline in $eCO_2(\text{ind})$. The statistically significant decreasing signal is mostly in boreal regions (16.8% of global vegetated land with $p < 0.05$) with hot spots in eastern Canada, Scandinavia, and south-central Siberia (Fig. 1c, d). Warm and wet climate zones show an opposite tendency with more limited significant patterns (9.9% of global vegetated land with $p < 0.05$) (Fig. 1c, d).

In parallel, we used satellite retrievals of near-infrared reflectance of vegetation (NIRv) as a proxy of observed GPP³² to further verify the robustness of the signals derived from model simulations. The satellite-observed $eCO_2(\text{ind})_{\text{obs}}$ was disentangled from the other confounding effects through a climate analog approach³³, based on the identification of years with similar climate and distinct atmospheric CO_2 concentration (details in Methods). Observation-based results confirm a global weakening effect of eCO_2 -driven climate change on GPP between the two periods (2000–2014 versus 1982–1996), with an overall change in $eCO_2(\text{ind})_{\text{obs}}$ of $-0.38 \text{ gC m}^{-2} \text{ ppm}^{-1}$. We also found a good agreement between model-based and observation-based results in terms of spatial patterns emerging across climatological and latitudinal gradients (Fig. 1d–f).

A comprehensive set of experiments was additionally performed to test whether our model-based results were potentially affected by the data source, temporal window length, and the criteria used to define the growing season (Supplementary Text 1 and 2; Supplementary Figs. 1 and 2, and Table 1). Meanwhile, analyses replicated by using the kernel normalized difference vegetation index (kNDVI) as an alternative satellite GPP proxy were also performed to further verify the robustness of our results (Supplementary Text 3; Supplementary Fig. 3). Altogether, these results univocally show a substantial reduction of the indirect effect of eCO_2 at the global scale (Fig. 1a and Supplementary Figs. 1–3) and particularly in the Northern Hemisphere (Fig. 1d–f and Supplementary Fig. 3c). Such patterns agree with the weakening temperature-vegetation relationship in northern ecosystems documented in previous literature²², and appear plausibly influenced by the increasing water limitation (Supplementary Fig. 4).

$eCO_2(\text{ind})$ is expected to further decline in all investigated future temporal periods under the SSP5-8.5 scenario to the point that the global mean could persistently settle on negative values (Fig. 2a). Five out of seven individual ESMs agree that eCO_2 -driven climate change will exert a negative role on the global vegetation carbon uptake for the period 2086–2100, albeit the inter-model spread is considerable (Supplementary Fig. 5a). For the period 2086–2100, the global $eCO_2(\text{ind})$ —as estimated by CMIP6_{SMA}—is projected to decrease significantly by $0.36 \text{ gC m}^{-2} \text{ ppm}^{-1}$ compared to the analogous estimate derived for the period 1982–1996 ($p < 0.01$, t test) (Fig. 2a). Such decreasing signal appears statistically significant ($p < 0.05$) over 46.5% of global vegetated land and prominently in the Northern Hemisphere (Fig. 2b,c). The global declining signal is partially dampened by opposite increasing patterns mainly occurring along the equatorial belt, which, however manifest statistically significant over a smaller extent (32.7%).

Table 1 | Information of CMIP6 ESMs used in this study

| Model name | Land surface component | Modeling center | Soil depth (m) |
|---------------|------------------------|---|----------------|
| ACCESS-ESM1-5 | CABLE2.4 with CASA-CNP | Commonwealth Scientific and Industrial Research Organisation, Australia | 2.872 |
| CanESM5 | CLASS-CTEM | Canadian Center for Climate Modeling and Analysis | 4.1 |
| CNRM-ESM2-1 | ISBA-CTRIP | Center National de Recherches Meteorologiques, France | 10 |
| E3SM-1-1 | ELM1.1 | U.S. Department of Energy | 35.18 |
| MIROC-ES2L | MATSIRO with VISIT-e | Japan Agency for Marine-Earth Science and Technology | 14 |
| MRI-ESM2-0 | HAL1.0 | Meteorological Research Institute of the Japan Meteorological Agency | 8.5 |
| UKESM1-0-LL | JULES-ES-1.0 | U.K. Natural Environment Research Council and Met Office | 2 |

Table 2 | Description of CMIP6 factorial simulations

| Simulation name | Type | Forcing constraints | | |
|----------------------------------|-------------------------------|---|---|--|
| | | CO ₂ radiative forcing | CO ₂ physiological forcing | Other forcings |
| historical (1850–2014) | Fully-coupled mode | Yes, CO ₂ increases from 285 ppm to 397 ppm | Yes, CO ₂ increases from 285 ppm to 397 ppm | Yes, factors including CH ₄ , N ₂ O, aerosols, and land use vary over time |
| hist-bgc (1850–2014) | Biogeochemically-coupled mode | No, CO ₂ fixed at 285 ppm (pre-industrial level) | Yes, CO ₂ increases from 285 ppm to 397 ppm | Yes, factors including CH ₄ , N ₂ O, aerosols, and land use vary over time |
| hist-CO ₂ (1850–2014) | Single-forcing mode | Yes, CO ₂ increases from 285 ppm to 397 ppm | Yes, CO ₂ increases from 285 ppm to 397 ppm | No, factors except CO ₂ fixed at the pre-industrial level |
| ssp585 (2015–2100) | Fully coupled mode | Yes, CO ₂ increases from 397 ppm to 1135 ppm | Yes, CO ₂ increases from 397 ppm to 1135 ppm | Yes, factors including CH ₄ , N ₂ O, aerosols, and land use vary over time |
| ssp585-bgc (2015–2100) | Biogeochemically coupled mode | No, CO ₂ fixed at 285 ppm (pre-industrial level) | Yes, CO ₂ increases from 397 ppm to 1135 ppm | Yes, factors including CH ₄ , N ₂ O, aerosols, and land use vary over time |

To derive a more comprehensive picture of the terrestrial ecosystem response to eCO₂-driven climate change, we explored the temporal change in the strength of indirect CO₂ effect on carbon release by respiration (Supplementary Fig. 6), and on the net ecosystem carbon uptake (eCO₂(ind)-NEP, Fig. 2d, e) through factorial experiments of CMIP6 ESMs. We estimated a global eCO₂(ind)-NEP of $-0.02 \text{ gC m}^{-2} \text{ ppm}^{-1}$ during the whole historical period (1982–2014), which is consistent with previous findings about the negative carbon-climate feedback from the land's perspective (i.e., positive from the atmosphere's perspective)³⁴. In pace with the attenuation of the indirect effect on total vegetation carbon uptake (Fig. 2a), global eCO₂(ind)-NEP is projected to decrease from $0.05 \pm 0.12 \text{ gC m}^{-2} \text{ ppm}^{-1}$ during 1982–1996 to $-0.05 \pm 0.03 \text{ gC m}^{-2} \text{ ppm}^{-1}$ during 2086–2100 (inset box in Fig. 2d). The smaller decline in eCO₂(ind)-NEP compared to that in eCO₂(ind) (-0.1 versus $-0.36 \text{ gC m}^{-2} \text{ ppm}^{-1}$) suggests the concurrently reduced influence on ecosystem respiration and its consequent offsetting effect. The latitudinal gradient of the changes in eCO₂(ind)-NEP between the two periods is largely concordant with the one derived from the changes in eCO₂(ind), thus reflecting similar spatial dependences on environmental factors (Fig. 2b–e).

Relationship between the indirect and direct effects of eCO₂

To quantify the relative importance of indirect versus direct effects of eCO₂ in regulating vegetation carbon uptake, simulated and observed eCO₂(dir) was derived based on a multiple non-linear regression (Methods) (i.e., CMIP6_{SMA} and obs-RM in Fig. 3a). The analyses were complemented by two additional independent estimates of eCO₂(dir) based on factorial experiments of CanESM5 (i.e., CanESM5-FE in Fig. 3a), and on the climate analog approach applied to observational datasets (i.e., obs in Fig. 3a) (details in Methods). We found that along with the decrease in eCO₂(ind), global eCO₂(dir) has dropped as well in recent years and is expected to further decline in the coming decades (Fig. 3a). Model results based on factorial experiments and non-linear regression show a strong reduction in global eCO₂(dir) between the periods 2000–2014 and 1982–1996, largely in agreement with satellite-derived estimates (Fig. 3a). Nevertheless, the magnitude of the decline simulated by CMIP6_{SMA} ($-0.44 \text{ gC m}^{-2} \text{ ppm}^{-1}$, or -22.8%) is clearly lower than the analogous estimate derived from satellite product (obs: $-1.20 \text{ gC m}^{-2} \text{ ppm}^{-1}$ or -78.3% ; obs-RM: $-1.65 \text{ gC m}^{-2} \text{ ppm}^{-1}$ or -67.0%) and from dedicated factorial experiments (CanESM5-FE: $-1.38 \text{ gC m}^{-2} \text{ ppm}^{-1}$ or -69.2%) (Fig. 3a). While we recognized the intrinsic difficulties of disentangling drivers and producing robust causal attribution in observation-based analysis, we argued the emerging differences between models and observations could be partially attributable to the simplifying assumptions of CMIP6 models.

Under the investigated SSP5-8.5 scenario, the relative importance of eCO₂(ind) and eCO₂(dir) for the terrestrial carbon cycle is expected to vary greatly. The relative contribution of eCO₂(ind) to the net effect of eCO₂ (i.e., eCO₂(net), the sum of eCO₂(dir) and eCO₂(ind)) will likely decrease from 11.1% (1982–11996) to -22.6% (2086–12100) (Fig. 3b). On the contrary, the relative contribution of eCO₂(dir) is projected to increase, mainly due to the higher relative decreasing rate of eCO₂(ind). However, in view of the expected progressive decline in both eCO₂(ind) and eCO₂(dir), eCO₂(net) could become negative, and eCO₂(ind) could emerge as the dominant driver of the future temporal dynamic of GPP. Some regions of the globe, such as central Canada, northern Amazon, and western and southern Africa, could exhibit a dominant role of eCO₂(ind) by the end of 21st century (Supplementary Fig. 7). A detailed analysis suggests that the negative eCO₂(ind) will overcome the positive eCO₂(dir) over 30.3% of global vegetated land by 2041–12055, and over 48.0% by 2086–12100 (Supplementary Fig. 8). These results agree with previous studies which have emphasized the expected net negative role of eCO₂ on the terrestrial carbon uptake as a result of the increasing detrimental impacts of climate change on vegetation and a saturating CO₂ fertilization¹³.

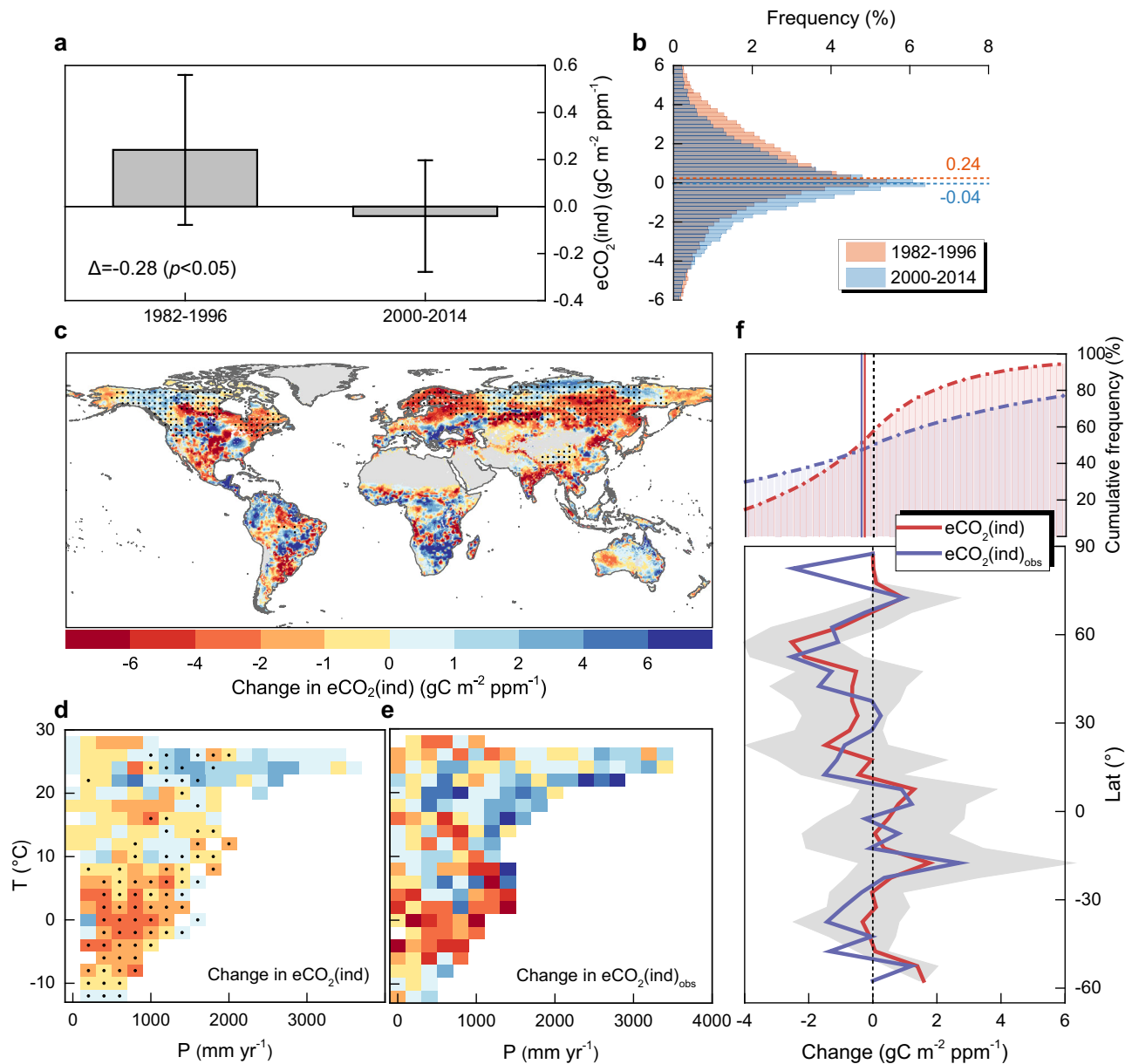


Fig. 1 | Historical variations in the indirect effect of elevated atmospheric CO₂ concentration (eCO₂) on vegetation carbon uptake. **a** Mean indirect effect of eCO₂ on growing-season gross primary production (GPP) via associated climate change (eCO₂(ind)) during the periods 1982–1996 and 2000–2014, as derived from the CMIP6 model ensemble (i.e., CMIP6_{SMA}). Error bars represent the standard error of effects derived from ensemble members (i.e., seven CMIP6 ESMS). Δ expresses the mean of difference in eCO₂(ind) between the two periods. The statistical significance of the difference is assessed by *t* test. **b** Frequency distribution of eCO₂(ind) at the global scale during the periods 1982–1996 and 2000–2014, as estimated with CMIP6_{SMA}. Distribution averages are shown as dotted horizontal lines. **c** Spatial pattern of difference in eCO₂(ind) between the two periods (2000–2014 versus 1982–1996) derived from CMIP6_{SMA}. Non-vegetated areas are excluded from our analysis and are shown in gray. Regions labeled by black dots indicate differences that are statistically significant (*t* test, $p < 0.05$). Dots are

spaced 3° in both latitude and longitude, and statistics were computed over 9° × 9° spatial moving windows. **d** Mean difference in eCO₂(ind) between the two periods (2000–2014 versus 1982–1996) simulated by CMIP6_{SMA}, binned as a function of climatological mean precipitation (P) and air temperature (T). Black dots indicate bins with differences that are statistically significant (*t* test, $p < 0.05$). **e** Same as **d**, but for eCO₂(ind)_{obs} which was estimated by the satellite-observed GPP_{obs} within a temporal climate analog framework. **f** Cumulative frequency distribution of difference in eCO₂(ind), and eCO₂(ind)_{obs} between the two periods (2000–2014 versus 1982–1996). Distribution averages are shown as solid vertical lines. The subplot below shows the zonal medians of difference in eCO₂(ind), and eCO₂(ind)_{obs} between the two periods (2000–2014 versus 1982–1996) at 5° latitudinal resolution. Corresponding interquartile ranges of CMIP6_{SMA} simulation are shown as shaded bands. Source data are provided as a Source Data file.

Results reveal that 66.9% of global vegetated land could experience the same direction of changes in eCO₂(ind) and eCO₂(dir) (i.e., “+ +” and “- -” in Fig. 3c) between the historical (1982–1996) and future (2086–2100, SSP5-8.5) period, while the remaining 33.1% could manifest reverse directions of changes (i.e., “+ -” and “- +”). The concurrent decrease in eCO₂(ind) and eCO₂(dir) (“- -”) appears to be the most pervasive case (48.5%), particularly over northern latitudes

(Fig. 3c). Averaged across regions with simultaneous reductions in eCO₂(ind) and eCO₂(dir), changes in eCO₂(ind) and eCO₂(dir) explain 47.9% and 52.1% of reduction in net CO₂ effect on growing-season GPP (-4.87 gC m⁻² ppm⁻¹), respectively (Fig. 3d). Such concurrent decrease in eCO₂(ind) and eCO₂(dir) is also reflected in the sharper decrease in eCO₂(net) in northern lands (-2.69 gC m⁻² ppm⁻¹, or -82.0%) between the historical and future periods compared to the global mean

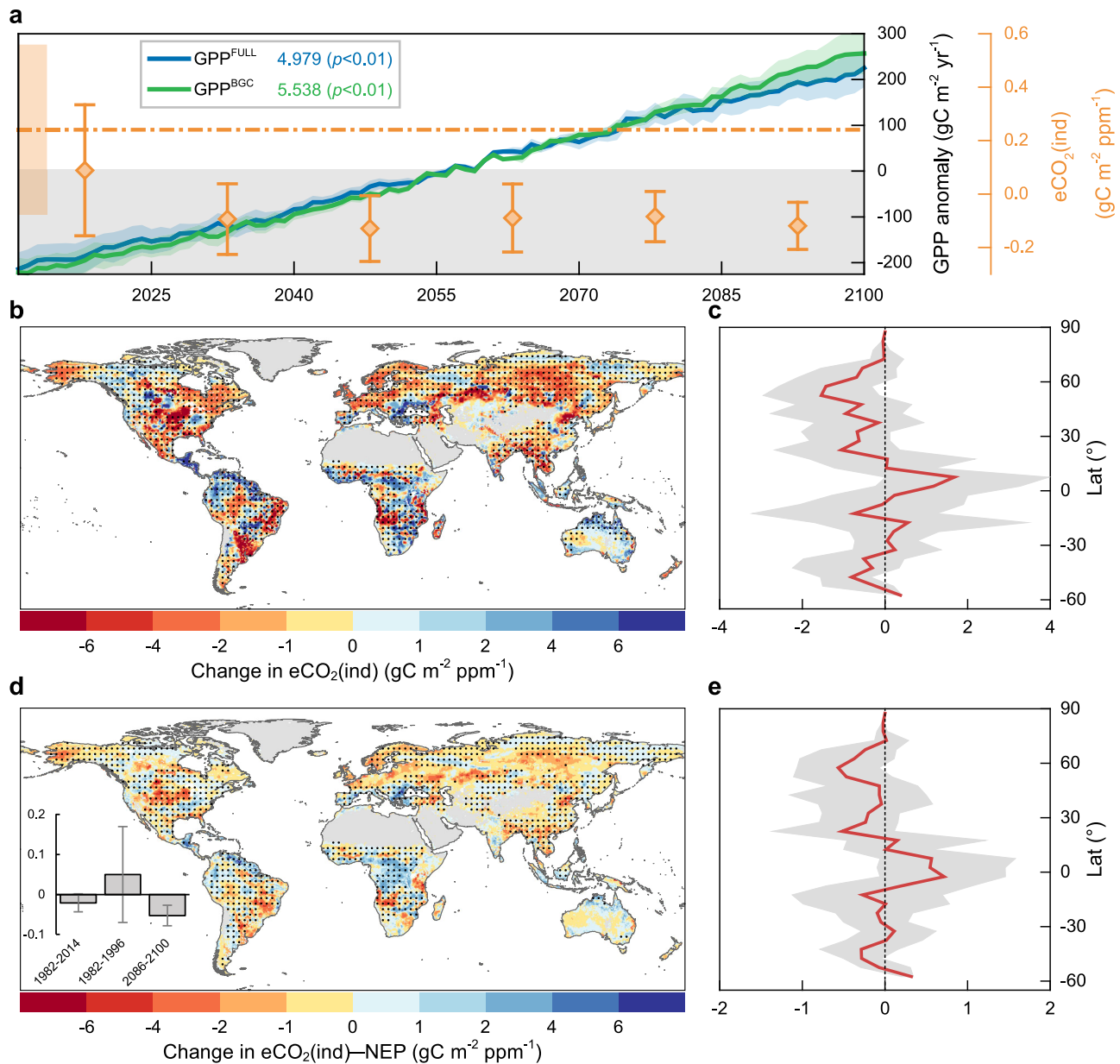


Fig. 2 | Projection of future variations in indirect effect of elevated atmospheric CO_2 concentration (eCO_2) on vegetation carbon uptake. **a Mean indirect effect of eCO_2 on growing-season gross primary production (GPP) via associated climate change ($\text{eCO}_2(\text{ind})$) derived from CMIP6_{SMA} during the six independent periods, namely 2011–2025, 2026–2040, 2041–2055, 2056–2070, 2071–2085, and 2086–2100. Ensemble mean and standard error are shown by the diamond symbol and whiskers, both referring to the right orange y axis. Dotted horizontal line and its shaded band represent the $\text{eCO}_2(\text{ind})$ during 1982–1996 and the corresponding standard error, as estimated by CMIP6_{SMA}. Interannual changes in anomalies of growing-season GPP over 2011–2100 globally, simulated by CMIP6_{SMA} under the fully-coupled experiment (GPP^{FULL}) and the biogeochemically-coupled experiment (GPP^{BGC}) are shown in blue and green lines, respectively. Numbers refer to the trends of GPP^{FULL} and GPP^{BGC} (unit: $\text{gC m}^{-2} \text{yr}^{-2}$) over 2011–2100. The statistical significance of trends is assessed by Mann–Kendall test. **b** Spatial pattern of difference**

in $\text{eCO}_2(\text{ind})$ between the historical and future periods (2086–2100 versus 1982–1996) derived from CMIP6_{SMA}. Regions labeled by black dots indicate differences that are statistically significant (t test, $p < 0.05$). Dots are spaced 3° in both latitude and longitude, and statistics were computed over $9^\circ \times 9^\circ$ spatial moving windows. **c** Zonal medians of difference in $\text{eCO}_2(\text{ind})$ between the historical and future periods (2086–2100 versus 1982–1996) simulated by CMIP6_{SMA} at 5° latitudinal resolution. Corresponding interquartile ranges of CMIP6_{SMA} simulation are shown as shaded band. **d, e** Same as **b, c** but for the indirect effect of eCO_2 on growing-season net ecosystem production (NEP) via associated climate change ($\text{eCO}_2(\text{ind}) - \text{NEP}$) derived from CMIP6_{SMA}. The inset in **d** shows the mean $\text{eCO}_2(\text{ind}) - \text{NEP}$ during the periods 1982–2014, 1982–1996, and 2086–2100, respectively. Error bars represent the standard error of effects derived from ensemble members. Source data are provided as a Source Data file.

($-1.65 \text{ gC m}^{-2} \text{ppm}^{-1}$, or -75.7%), as estimated by CMIP6_{SMA} (Supplementary Table 2).

Additional analyses based on model simulations from the idealized 1% per year increasing CO_2 experiments show spatial patterns and trends in both indirect and direct CO_2 effects at the global mean level similar to those described above (Supplementary Text 4;

Supplementary Figs. 9–11). Meanwhile, under such idealized scenario where radiatively-coupled mode is available, estimates of direct CO_2 effect based on the non-linear regression framework and those based on the climate analog approach were carefully compared against those obtained directly from factorial experiments (Supplementary Text 4). The high agreement among the three sets of estimates further

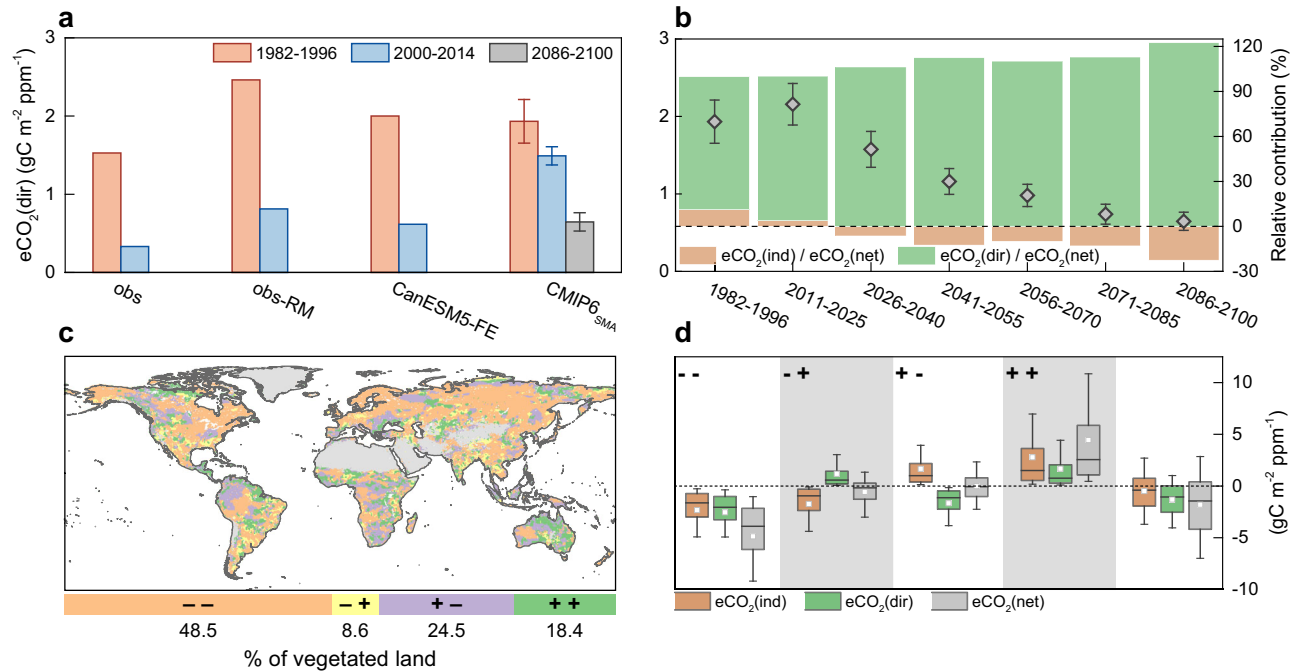


Fig. 3 | Relationship between direct and indirect effects of elevated atmospheric CO₂ concentration (eCO₂) on vegetation carbon uptake. **a** Mean direct physiological effect of eCO₂ on growing-season gross primary production (GPP) (eCO₂(dir)) during periods 1982–1996 and 2000–2014, simulated by CanESM5 factorial experiments (i.e., CanESM5-FE), and estimated by observed GPP under the temporal climate analog framework (i.e., obs), estimated by observed GPP in combination with the non-linear regression model (i.e., obs-RM), and estimated by CMIP6_{SMA}-simulated GPP in combination with the non-linear regression model (i.e., CMIP6_{SMA}). Mean eCO₂(dir) during the period 2086–2100 under SSP5-8.5 projected by CMIP6_{SMA} is also provided. Error bars represent the standard error of effects derived from ensemble members (i.e., seven CMIP6 ESMS). **b** Mean eCO₂(dir) derived from CMIP6_{SMA} and its standard error during seven independent periods, namely 1982–1996, 2011–2025, 2026–2040, 2041–2055, 2056–2070, 2071–2085, and 2086–2100, shown by diamond symbol and whiskers. Bars in green

and orange represent the relative contributions of the indirect effect of eCO₂ (eCO₂(ind)) and eCO₂(dir) to the net effect of eCO₂ (eCO₂(net)) during corresponding periods and derived from CMIP6_{SMA}. **c** Spatial pattern of relationship between changes in eCO₂(ind) and eCO₂(dir) between historical and future periods (2086–2100 versus 1982–1996), where “--” represents decrease in eCO₂(ind) and decrease in eCO₂(dir), “-+” represents decrease in eCO₂(ind) and increase in eCO₂(dir) and so on. The legend shows the fraction of vegetated areas for each thematic class (i.e., “--”, “-+”, “+-”, and “++”). **d** Boxplot of changes in eCO₂(ind), eCO₂(dir), and eCO₂(net) between historical and future periods (2086–2100 versus 1982–1996) for different thematic classes mentioned in **c** and for the globe (rightmost). Boxplot elements: box = values of 25th and 75th percentiles; horizontal line = median; rectangle = mean; whiskers = values of 10th and 90th percentiles. Source data are provided as a Source Data file.

supports the validity of our multiple non-linear regression framework and of the climate analog approach (Supplementary Figs. 12 and 13).

GPP in the Northern Hemisphere has increased steadily during the past decades³⁵ in response to the large and positive eCO₂(ind) and eCO₂(dir) (Supplementary Fig. 14), thus playing a critical contribution to the global terrestrial carbon sink^{36,37}. Therefore, the widespread and strong decrease in both indirect and direct effects of eCO₂ in the Northern Hemisphere resulting from our analyses rises concern about the future dynamic of the regional carbon sink and its capacity to keep the pace of anthropogenic emissions.

Mechanisms behind the decline in the indirect effect of eCO₂

To disentangle the possible mechanisms responsible for the declining eCO₂(ind), we explored its relationship with the expected changes in terrestrial water availability. To this aim, we first exploited the CMIP6 simulations to quantify the spatiotemporal variations in aridity conditions, here expressed in terms of surface (0–10 cm) soil moisture (SM_{surf}). Results indicate a projected widespread decline in terrestrial water availability by the end of the century compared to the current conditions (82.6% of global vegetated land exposed to a reduction in SM_{surf}, Fig. 4a). At the global level and based on multi-model means (i.e., CMIP6_{SMA}), we estimated a significant decrease in SM_{surf} during 2086–2100 by 7.3% ($p < 0.01$, t -test) compared to analogous estimates obtained for the period 1982–1996 (Fig. 4b). Similar drying patterns emerge for individual model runs (Supplementary Fig. 15), for total soil moisture (SM_{total}), for a widely used aridity index (defined as the ratio

of annual precipitation to potential evapotranspiration, P/PET) (Supplementary Figs. 16 and 17). Previous studies focusing on dryness indices³⁸ and hydrological regimes^{39,40} further corroborate such drying trends.

To investigate the relationship between change in eCO₂(ind) and land surface drying/wetting, we averaged the change in eCO₂(ind) across gradients of mean annual SM_{surf} during 1982–1996 and the corresponding change in SM_{surf} (i.e., 2000–2014 versus 1982–1996, and 2086–2100 versus 1982–1996). SM_{surf} = 0.26 m³ m⁻³ generally corresponds to P/PET = 1 at the mean annual scale (Supplementary Fig. 17b), which is widely treated as the threshold between non-humid and humid regions^{41,42}. We found that eCO₂(ind) generally declines (enhances) with the land drying (wetting) in humid regions (SM_{surf} > 0.26 m³ m⁻³, Supplementary Fig. 4a) in both historical and scenario simulations (Fig. 4c, d). However, in water-limited conditions (SM_{surf} < 0.26 m³ m⁻³), the weakened negative eCO₂(ind) along with the land drying results in a negative relationship between changes in eCO₂(ind) and SM_{surf} (Fig. 4c, d and Supplementary Fig. 7). CO₂ and drought-related enhancement in growing-season water-use efficiency (WUE) (Supplementary Fig. 18), relax the water limitation to vegetation growth, especially over semi-arid climate zones^{24,43–45}, and may consequently limit the negative trend in eCO₂(ind) (Fig. 4d). In addition, for water-limited environments, a decrease in eCO₂(ind) occurs consistently under both land drying and wetting, indicating the possible importance of other factors, such as vegetation type and species diversity, in modulating the vegetation response to climate change.

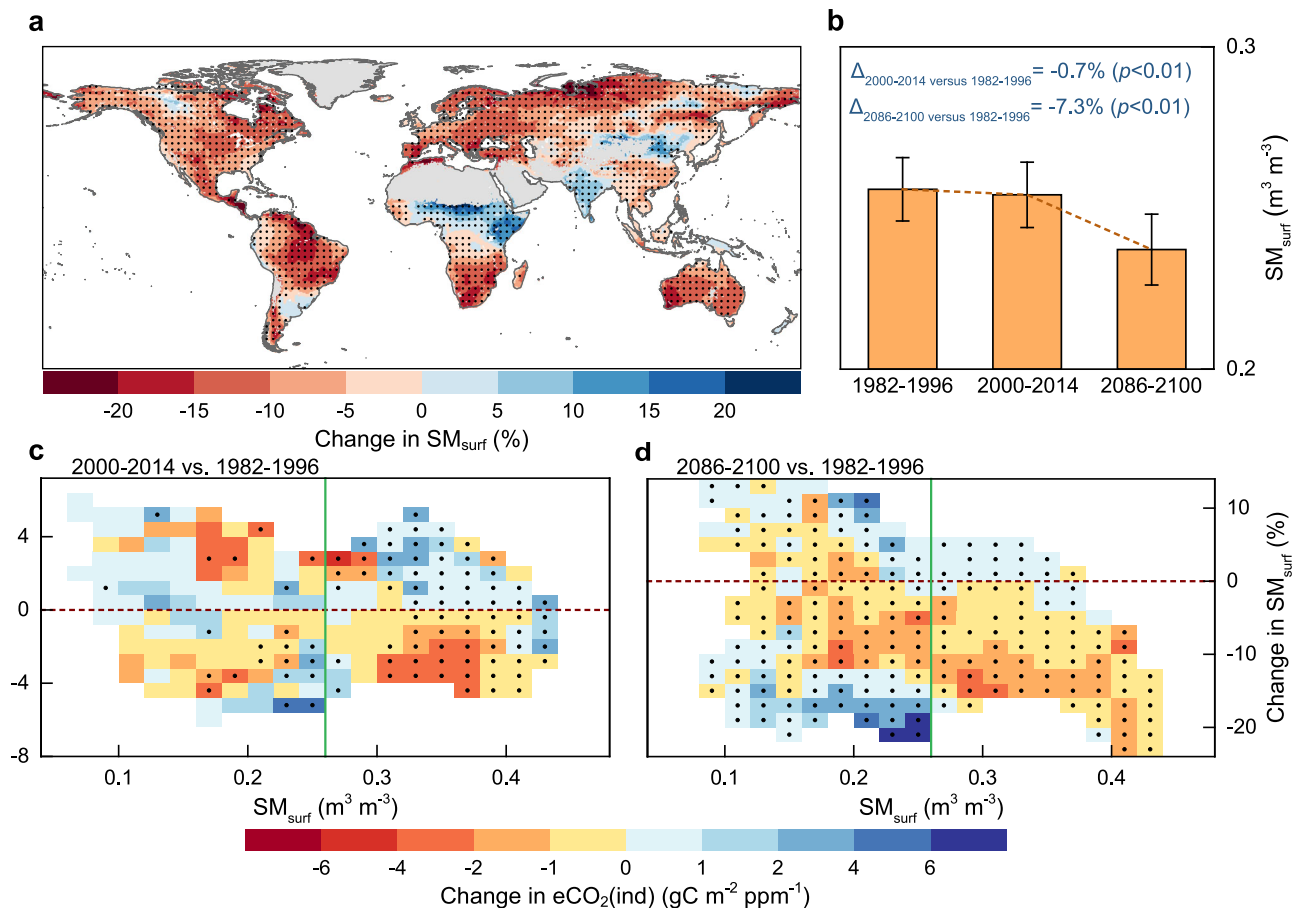


Fig. 4 | Sensitivity of indirect CO₂ effect on terrestrial water availability.

a Spatial pattern of relative change in surface soil moisture (SM_{surf}) between the historical and future periods (2086–2100 versus 1982–1996) derived from CMIP6_{SMA}. Regions labeled by black dots indicate changes that are statistically significant (t test, $p < 0.05$). Dots are spaced 3° in both latitude and longitude, and statistics were computed over $9^\circ \times 9^\circ$ spatial moving windows. **b** Global mean SM_{surf} derived from CMIP6_{SMA} during the period 1982–1996, 2000–2014, and 2086–2100, respectively. Numbers refer to change in SM_{surf} relative to 1982–2016. **c** Difference in indirect effect of elevated atmospheric CO₂ concentration (eCO_2) on growing-season gross primary production (GPP) via associated climate change

($eCO_2(ind)$) between the periods 1982–1996 and 2000–2014 derived from CMIP6_{SMA}, binned as a function of corresponding changes in SM_{surf} and mean annual SM_{surf} (Supplementary Fig. 4a). $SM_{surf} = 0.26 m^3 m^{-3}$ (i.e., the green solid line) overall corresponds to the ratio of annual precipitation to potential evapotranspiration (P/PET) = 1 at the mean annual scale, that is the threshold between non-humid and humid regions (Supplementary Fig. 17b). Black dots indicate bins with differences that are statistically significant (t test, $p < 0.05$). **d** Same as **c**, but for the difference between the periods 1982–1996 and 2086–2100. Source data are provided as a Source Data file.

Similar sensitivities to increasing water limitation have been obtained using SM_{total} and P/PET in place of SM_{surf} and referring to different temporal window lengths (Supplementary Figs. 16, 17, and 19). Such high consistency demonstrates the substantial independence of our results on the proxy of terrestrial water availability and the selection of time-window length.

Discussion

Our study provides multiple and coherent evidence that the indirect effect of eCO_2 on global vegetation carbon uptake via associated climate change has declined over the last three decades (Fig. 1 and Supplementary Fig. 3). The signal of the ongoing trends has been derived both from Earth system models' simulations and from satellite observations using a statistical approach to disentangle direct and indirect CO₂ effects from time series analysis. In addition, results show that the positive indirect effect of eCO_2 that has stimulated the global GPP in recent years will most likely continue to decline in the future, particularly in northern high latitudes, and turn into negative values firmly under the high CO₂ emission scenario (Fig. 2). This epochal change in the sign of the indirect CO₂ effect may lead to a positive land carbon-climate feedback from the atmosphere's perspective^{34,46}.

The interpretation of the CO₂ effects mediated by climate change is intrinsically complex because primary productivity is controlled by different environmental drivers in the different biomes, like low temperature in the boreal regions, incoming radiation in the humid tropics, or water availability in the arid regions²⁷. For this reason, analyses have to address multiple factors and their interactions at once^{28,47}. However, previous assessments were largely based on the analysis of a single climatic factor (e.g., temperature²², water availability⁴⁸, and VPD²³), while our study presents an attempt to integrate multiple drivers across the different World regions. For instance, the strong signal emerging in the boreal regions (Figs. 1f and 2c) can be partially attributable to the weakening temperature-vegetation relationship in northern ecosystems²², which may be related to the non-linear response of photosynthesis to temperature, increased extreme heat, increasing water limitation driven by the anticipation of phenology⁴⁹ and expansion of woody shrubs^{50,51}.

Our assessment shows that the increasing water limitation is a critical driver of the weakened indirect effect of eCO_2 on the global vegetation carbon uptake (Fig. 4 and Supplementary Figs. 16, 17 and 19). This phenomena may be driven by the detrimental effect of water

scarcity on the resilience of global vegetation to climate variability and extremes⁵². An exception to this pattern occurs in water-limited environments, where the negative indirect effect of eCO₂ seems to weaken with the land drying (Fig. 4c, d), probably due to the enhancement of direct CO₂ effect on WUE and the resulting mitigating effect on water constraints²⁴ (Supplementary Fig. 18). A recent analysis focusing on global forests suggests that WUE and aridity index are closely and negatively related below a threshold value of aridity index ≈ 1⁵³, partly supporting our finding.

The complex interplay between the rapid changes in climate conditions and the increasing risks of natural disturbances may also contribute to the transition from positive to negative indirect CO₂ effects. For example, warmer and drier conditions facilitate insect outbreaks, while warmer and wetter conditions increase disturbance from pathogens⁵⁴. The expected intensification of disturbances may amplify the negative effect of climate change on primary productivity by enhancing plant vulnerability and mortality rates⁵⁵. However, the abovementioned processes have not yet been fully considered in state-of-the-art dynamic vegetation models and ESMs that are used in major climate assessments like the Intergovernmental Panel on Climate Change (IPCC) Assessment Reports^{56,57}. The simplified representation of disturbances and mortality in these models may ultimately hamper our full understanding of the ongoing and future variations in carbon-climate feedback, and in turn, lead to the overestimation of the future terrestrial carbon sink due to the misestimation of the indirect effect of eCO₂. In fact, our study shows that CMIP6 model simulations clearly report a lower magnitude of the decline in global indirect CO₂ effect during the historical period compared with observation-based estimates (Fig. 1f). This could be attributable to the poor representation of water limitation and natural disturbances in current ESMs, the limited consideration of vegetation mortality associated with biotic agents and the non-linearity of the processes behind^{57,58}. Considering that disturbance regimes are expected to intensify in many parts of the globe because of climate change^{54,58,59}, the enhanced representation of the phenomena in ESMs would plausibly produce an even stronger decline in the global projection of the indirect CO₂ effect.

The weakened indirect effect of eCO₂ reported here, in addition to the concurrent decline in direct physiological effect, confirms the transitory nature of the strong growth benefits induced by climate warming and CO₂ fertilization, especially in the boreal regions^{9,60}. These findings are in accordance with the expectation about the future saturation of CO₂ fertilization effect and the increasingly negative effect of climate change on vegetation¹³. More importantly, the simultaneous reductions in indirect and direct effects of eCO₂ imply that eCO₂ may exert a less positive up to negative role on the terrestrial carbon uptake in the future (Fig. 3), consequently reducing the ecosystems' capacity to sequester atmospheric CO₂. These phenomena may ultimately lead to an acceleration of climate change in the second part of the century, further challenging the efforts of humanity toward carbon neutrality. In addition, more frequent and severe climate extremes in a warming climate^{61,62}, e.g., increasing drought conditions, may further aggravate the decline in the indirect effect of eCO₂ (Fig. 4) as well as that in direct CO₂ fertilization⁶³. The intensification of a positive feedback loop between climate change and land CO₂ emission undoubtedly would limit the potential of terrestrial ecosystems to serve as carbon sinks and have great implications for the efficacy of land-based mitigation policies and for the societal efforts required for meeting climate mitigation targets. In this respect, our results contribute to a better understanding of global change impacts on terrestrial ecosystems under current and future conditions, and meanwhile, may help the development of more integrated and realistic mitigation strategies, by informing climate policies on the weakening of the fertilization effects of eCO₂ and associated amplification of climate warming.

Methods

CMIP6 simulations

To explore the indirect effect of eCO₂ on vegetation carbon uptake, we used outputs from an ensemble of seven Earth system models (ESMs) that participate in the carbon-climate feedback experiment (C4MIP) within the framework of the Coupled Model Intercomparison Project Phase 6 (CMIP6)³⁰ (<https://esgf-node.llnl.gov/search/cmip6/>): ACCESS-ESM1-5, CanESM5, CNRM-ESM2-1, E3SM-1-1, MIROC-ES2L, MRI-ESM2-0, and UKESM1-0-LL (Table 1). These models were selected because they provide simulations under different coupling modes required to disentangle the effects of eCO₂. We focused on the SSP5-8.5 scenario because C4MIP simulations are available only for the highest emission trajectory (CO₂ concentration is projected to reach 1135 ppm in 2100⁶⁴). The ESMs have full carbon cycles, which include carbon uptake by vegetation that varies in response to changes in atmospheric CO₂ concentration and climate⁴⁶. For each ESM, one biogeochemically-coupled experiment and one fully-coupled experiment in both historical (1982–2014) and future scenario (2015–2100) periods were analyzed within a factorial simulation framework (Table 2). In biogeochemically coupled experiments (“hist-bgc” and “ssp585-bgc” in the CMIP6 terminology), biogeochemical processes over land respond to eCO₂, whereas the radiative code experiences fixed CO₂. In the fully-coupled experiment (“historical” and “ssp585” in the CMIP6 terminology), both radiative and biogeochemical processes respond to eCO₂ (consistent with observations in the historical period). All other forcings (e.g., non-CO₂ greenhouse gases, aerosols, and land use) are identical for these two sets of experiments, i.e., time-varying in both radiative and biogeochemical processes. Furthermore, we used outputs from CO₂ individual forcing experiment (“hist-CO₂” in the CMIP6 terminology) conducted by the Detection and Attribution Model Intercomparison Project (DAMIP)⁶⁵ (Table 2). “hist-CO₂” experiment refers to the historical simulation driven only by observed changes in CO₂ concentration, with other forcings keeping temporally constant (e.g., non-CO₂ greenhouse gases, aerosols, and land use). Combining “hist-CO₂” with “historical” and “hist-bgc” enables to quantify the historical eCO₂(dir) through factorial simulations of CMIP6 runs. Unfortunately, CO₂ individual forcing experiment has not yet been extended to the future period, and only one ESM (i.e., CanESM5) took part in all three experiments. Because of these disadvantages, the abovementioned analysis applied for the estimation of global direct effects of eCO₂ was complemented by a more general regression framework extendible to the full ESM ensemble and to the different temporal periods (details in section “Quantifying indirect and direct effects of eCO₂ by model outputs”). Factorial simulations based on the abovementioned experiments (“hist-bgc”, “historical”, and “hist-CO₂”) were elaborated in the following sections.

A set of variables generated by ESM simulations were used for the following analyses, including: monthly scale gross primary production (GPP), net primary production (NPP), autotrophic respiration (R_a), heterotrophic respiration (R_h), evapotranspiration (ET), maximum, minimum and mean air temperature (T_{max} , T_{min} , and T), precipitation (P), cloud cover (CL), relative humidity (RH), surface (0–10 cm) soil moisture (SM_{surf} , 0–10 cm), and total soil moisture (SM_{total} , depth depending on models, see Table 1). Considering that the hydrologically active soil depth varies greatly among the models (from 2 m in UKESM1-0-LL to 35.18 m in E3SM-1-1), SM_{total} as well as SM_{surf} was converted from the original gravimetric unit ($kg\ m^{-2}$) to volumetric unit ($m^3\ m^{-3}$) by dividing the gravimetric soil water content by the corresponding soil depth. Such conversion allows for the comparison of results obtained from different models and the development of more robust multi-model ensembles of soil moisture. Variations in SM_{total} and SM_{surf} were expressed in relative terms (%) with respect to their average values computed for the baseline period (e.g., 1982–1996)³⁹ (Fig. 4 and Supplementary Figs. 4, 15 and 16). Only for the E3SM-1-1 model, some of the abovementioned variables were not

provided (NPP, T_{\max} , T_{\min} , and RH), and therefore they were retrieved by empirical formula and statistical approach (additional details reported in Supplementary Text 5). We additionally derived ecosystem respiration (R_{eco}) as the sum of R_a and R_h , and the net ecosystem production (NEP) was calculated as the difference between GPP and R_{eco} ⁶⁶. Vapor pressure deficit (VPD), which directly relates to atmospheric water demand^{19,67}, was calculated based on Abbott and Tabony⁶⁸ for each grid-cell as follows:

$$\text{VPD} = 0.6108e^{\frac{17.27T}{T+237.3}} \left(1 - \frac{\text{RH}}{100}\right) \quad (1)$$

where T is given in °C, and the resulting VPD is in kPa. Furthermore, we used the ratio of mean annual P to potential evapotranspiration (PET) as the aridity index retrieved from the FAO Penman-Monteith algorithm⁶⁹. Details on the PET estimation are reported in Supplementary Text 6.

CMIP6 outputs were resampled to a common $0.5^\circ \times 0.5^\circ$ global grid-cell using the bilinear method of interpolation. Moreover, for each temporal window (e.g., 1982–1996, 2000–2014, 2086–2100, and 1982–2014), we computed the associated multi-year mean growing season at the grid-cell scale. The growing season was defined as the period spanning months with average $T > 0^\circ\text{C}$ ¹⁴ and—limitedly to arid and semi-arid ecosystems—cumulative P between 10% and 90% of the annual total P (Supplementary Fig. 20). The integration of a P threshold in the definition of the growing season for water-limited environments enables to account for possible inactive vegetation phase at $T > 0^\circ\text{C}$ due to water deficit conditions⁷⁰. Areas characterized by an aridity index, quantified in terms of P/PET, < 1 were labeled as arid and semi-arid ecosystems⁹. For arid and semi-arid grid cells located in the Southern Hemisphere, P accumulation was set to start in July and end in June of the next year. The resulting growing season was used as a reference period to aggregate the original monthly variables provided by CMIP6 to the growing-season scale. The robustness of our results is tested with respect to two alternative definitions of the growing season period: (1) $T > 5^\circ\text{C}$ and cumulative P between 10% and 90% of the annual total P; (2) $T > 5^\circ\text{C}$ and cumulative P between 20% and 80% of the annual total P (Supplementary Fig. 2). In both cases, the P threshold is applied to arid and semi-arid regions only.

Observation-based products

We exploited the long-term GPP dataset (hereafter GPP_{obs}) based on near-infrared reflectance of vegetation (NIRv) retrieved from the Advanced Very High Resolution Radiometer (AVHRR) reflectance observations^{32,71} (<https://data.tpdc.ac.cn/en/data/d6dff40f-5dbd-4fd2-ac96-55827ab93cc5/>). The satellite GPP dataset, provided at monthly temporal resolution and at 0.05° spatial resolution, has global coverage and spans the period 1982–2014 (Supplementary Fig. 21a). It has been largely validated in previous studies against ground measurements and compared with estimates derived from machine-learning upscaling approaches, light-use-efficiency models and processed-based models^{32,72}. To match the spatial and temporal resolution of ESMS output, satellite GPP data were resampled to 0.5° and integrated over the growing season derived from the CMIP6 simulations in the fully-coupled experiment, as described above, to increase consistency in the data-model comparison (Supplementary Fig. 20). The obtained satellite-based growing season GPP data were used to evaluate the ESMS performance in capturing global GPP dynamics (Supplementary Figs. 22 and 23).

Furthermore, to explore the observed impact of eCO_2 on vegetation carbon uptake (details in the following sections), we used monthly T_{\max} , T_{\min} , T , P , CL, actual water vapor (VP), and PET retrieved from the Climatic Research Unit (CRU v4.05) climate dataset⁷³ (<https://catalogue.ceda.ac.uk/>) delivered for the whole globe at 0.5° spatial resolution and covering the period 1982–2014.

We additionally derived monthly VPD values as the difference between the saturated vapor pressure (SVP) and VP for each grid-cell based on the following formulation:

$$\text{VPD} = 0.6108e^{\frac{17.27T}{T+237.3}} - \text{VP} \quad (2)$$

where T is given in °C, VP and VPD are in kPa. Here we applied Eq. (2) instead of Eq. (1) to estimate VPD because RH is not available from the CRU dataset. All climatic factors were then aggregated at the growing-season temporal resolution.

We derived a global vegetated land mask from the annual land cover maps of the European Space Agency's Climate Change Initiative⁷⁴ (<https://www.esa-landcover-cci.org>) acquired for the period 1992–2014 at 300 m spatial resolution, referring to a simplified aggregation scheme based on physiognomy alone. Land cover maps were resampled to 0.5° using the majority method to match the common spatial resolution. All grid cells ($0.5 \times 0.5^\circ$ resolution) classified as vegetation class (including forest, grassland, shrubland, cropland, and wetland) throughout the 23 years were defined as vegetated areas and included in our analyses (Supplementary Fig. 24).

Assessing indirect/direct effects of eCO_2 from model outputs

Following similar approaches reported in literature^{10,16,75,76}, the effect of eCO_2 -induced climate change on growing-season GPP (i.e., the indirect effect of eCO_2 , expressed as $\text{eCO}_2(\text{ind})$) was derived from factorial simulations of multiple CMIP6 experiments by calculating the difference between the trend in growing-season GPP generated in the fully-coupled mode and that in the biogeochemically-coupled mode normalized by the increase rate of atmospheric CO_2 concentration:

$$\text{eCO}_2(\text{ind}) = \frac{\delta\text{GPP}^{\text{FULL}} - \delta\text{GPP}^{\text{BGC}}}{\delta\text{CO}_2} \quad (3)$$

where $\delta\text{GPP}^{\text{FULL}}$ and $\delta\text{GPP}^{\text{BGC}}$ are the trends in growing-season GPP in the fully-coupled experiment (i.e., “historical” and “ssp585”) and the biogeochemically-coupled experiment (i.e., “hist-bgc” and “ssp585-bgc”), respectively; δCO_2 represents the trend in atmospheric CO_2 concentration and is prescribed by CMIP6^{64,77}. The statistical significance of the trends was evaluated using the nonparametric Mann–Kendall test. The absolute signal (term $\delta\text{GPP}^{\text{FULL}} - \delta\text{GPP}^{\text{BGC}}$) was normalized to the unit of $\text{gC m}^{-2} \text{ppm}^{-1}$, to eliminate the impact of the difference in increasing rate of atmospheric CO_2 concentration in various periods (e.g., 1982–1996, 2000–2014, and 2086–2100). The term $\text{eCO}_2(\text{ind})$ excludes the direct physiological effect of eCO_2 and the effects of non- CO_2 forcing agents on GPP, as these components have been removed from the factorial simulations (Eq. (3)). The approach enabled us to separately quantify the $\text{eCO}_2(\text{ind})$ for different reference temporal period (e.g., 1982–1996, 2000–2014, and 2086–2100) at grid-cell level. For global-scale $\text{eCO}_2(\text{ind})$ estimates, the GPP terms reported in (Eq. (3)) were obtained by spatial average weighting each grid-cell value based on its area (Fig. 1a). The same methodology is applied consistently for all global-scale and regional-scale aggregated metrics described in the following sections. The analyses were complemented by applying Eq. (3) to NPP, R_a , R_h , R_{eco} , and NEP (in place of GPP) to comprehensively evaluate the response of distinct carbon fluxes to CO_2 radiative forcing (Fig. 2d, e and Supplementary Fig. 6).

We quantified the direct effect of eCO_2 on growing-season GPP (i.e., $\text{eCO}_2(\text{dir})$) within a multiple non-linear regression framework applied to simulations obtained from the CMIP6 fully-coupled experiment. Such approach was specifically designed since radiatively-coupled experiments ideally required to derive $\text{eCO}_2(\text{dir})$ from factorial simulations were not available. To derive robust fitting functions, we first performed a collinearity test based on the variance inflation factor (VIF), to preliminary select what drivers to include in

the multiple regression. Results show that CO₂, T_{min}, P, VPD, and CL, show no/weak collinearity (VIF < 10) in most parts of the globe (CRU: 97.0–100%; CMIP_{SMA}: 86.7–100%) and thus were all retained in the predictor set (Supplementary Fig. 25). Considering that climate exerts non-linear control on terrestrial carbon uptake^{78,79}, non-linear terms (e.g., interaction and quadratic terms) were incorporated into the regression model in addition to linear terms. Following the modeling framework described in Chen et al.⁸⁰, we used stepwise regression at the grid-cell scale to reduce redundant predictors. The model form most often identified across all grid cells was ultimately adopted to each grid-cell, enabling a consistent analysis at the global scale. The adopted model is described by the following equation:

$$\text{GPP} = \beta(\text{CO}_2) + C_1(P) + C_2(\text{VPD}) + C_3(T_{\min} \cdot \text{VPD}) + C_4(P \cdot \text{CL}) + C_5 + \varepsilon \quad (4)$$

where β , C_1 , C_2 , C_3 , C_4 , and C_5 represent the regression coefficients, and ε is the residual error term. Therein, β (gC m⁻² ppm⁻¹) refers to the sensitivity of GPP to CO₂, and thus reflects the term eCO₂(dir). Such an approach enabled us to disentangle the direct physiological effect of eCO₂ on GPP by factoring out the potentially confounding effects of climatic factors. All variables in Eq. (4) were taken from CMIP6 model simulations under “historical” and “ssp585” experiments. Regressions were estimated on annual anomalies (i.e., annual values minus the mean signal for a given period) for all variables, thus removing the background effects on vegetation but preserving those originating from interannual variations⁹. We performed an additional set of modeling experiments to test the model sensitivity on different hydrological variables. To this aim, we expressed the interannual variations in GPP within a non-linear regression that incorporates soil moisture in place of P (details in Supplementary Text 7). Test results based on the Akaike Information Criterion (AIC), the corrected Akaike Information Criterion (AICc), and the Bayesian Information Criterion (BIC) suggest that non-linear regression based on soil moisture has no substantial improvement in model performance (Supplementary Fig. 26) and leads to larger inter-model spread compared to the original one (i.e., Eq. (4)) (Supplementary Fig. 27 and Table 3). We therefore retained the regression framework based on P as defined in Eq. (4) for subsequent analyses.

For CanESM5, we estimated eCO₂(dir) by the use of an alternative method based on the outputs from three sets of factorial experiments available for the historical period as follows:

$$\text{eCO}_2(\text{dir}) = \frac{\delta\text{GPP}^{\text{CO}_2} - (\delta\text{GPP}^{\text{FULL}} - \delta\text{GPP}^{\text{BGC}})}{\delta\text{CO}_2} \quad (5)$$

where $\delta\text{GPP}^{\text{CO}_2}$ is the trend in growing-season GPP in the CO₂ individual forcing experiment (“hist-CO₂”). Estimates based on this approach were compared against those generated by the above-mentioned regression model to test the robustness of Eq. (4) in quantifying global mean eCO₂(dir) and its change (Fig. 3a).

Deriving indirect effect of eCO₂ from observations

To further corroborate our model-based findings, we investigated the direct and indirect components of eCO₂ and their changes through an observation-based approach. The method is based on the pixel-level assessment of the changes in GPP under similar climate conditions but different atmospheric CO₂ concentrations. For this purpose, we used the climate analog approach³³ to identify couples of years with different atmospheric CO₂ concentrations but similar climate conditions (i.e., climate analogous (CA) years) in each time period (e.g., 1982–1996, and 2000–2014) based on the CRU v4.05 climate dataset. Temporal climate analogs are derived from the Mahalanobis distance, which is a multivariate distance independent of the scale of the climate variables⁸¹. For the period 1982–1996, as an example, we first identified the two sub-periods 1982–1988 and 1989–1996, and then identified for

each grid-cell the years in which the climate condition is most similar between the two sub-periods. We calculated the Mahalanobis distance based on eleven climate variables derived from the CRU v4.05 dataset and identified as key determinants for climate analog analysis in previous studies^{33,81–83}. The selected variables include: mean annual CL, mean annual VPD, mean annual T , total annual P , annual P/PET, mean T , and total P for December–February (DJF) and June–August (JJA), T seasonality (represented by the standard deviation of monthly T), and P seasonality (represented by the coefficient of variation in monthly P). In order to reduce the dimensionality of the data space, we applied a principal component analysis to all climate variables and discarded the principal components with variance < 0.01³³. The Mahalanobis distance was then computed between all the possible 56-member couples of years at the grid-cell scale based on the following equation:

$$\text{MD}_{ij} = \sqrt{\sum_{k=1}^N \frac{(x_{jk} - x_{ik})^2}{\sigma_k^2}} \quad (6)$$

where j and i belong to the first and second sub-period, respectively; x_{jm} and x_{im} are the values of the principal component k in the year j and i , N represents the number of retained principal components, and σ_k^2 refers to the standard deviation of the principal component k . Low MD scores represent similar climate conditions between the two sub-periods, high MD scores the opposite. For each grid-cell, the minimum Mahalanobis distance (MD_{min}) was then selected, and its corresponding couple of years were identified as potential CA years.

We assessed the statistical significance of the obtained MD_{min}. Considering that the chi distribution provides a null distribution for (non-squared) Mahalanobis distances, the obtained MD_{min} can be expressed probabilistically as percentiles of a *chi* distribution with degrees of freedom corresponding to the number of dimensions in which MD_{min} was measured (i.e., N in Eq. (6)). Following Mahony et al.³³, we considered the 95th percentile of the associated *chi* distribution to identify the upper threshold of the representative analog. MD_{min} whose corresponding percentile is lower than the above-mentioned threshold, indicates a statistically similar climate between those two years (i.e., CA years).

Climate analogs were found not significant for a minority of grid cells (4.2%), and these areas were therefore excluded from the following analyses. For the remaining grid cells, we estimated the direct physiological effect of eCO₂ on GPP as follows:

$$\text{eCO}_2(\text{dir})_{\text{obs}} = \frac{\Delta\text{GPP}_{\text{obs}}^{\text{CA}}}{\Delta\text{CO}_2^{\text{CA}}} \quad (7)$$

where $\Delta\text{GPP}_{\text{obs}}^{\text{CA}}$ is the change in growing-season GPP_{obs} computed between CA years, and $\Delta\text{CO}_2^{\text{CA}}$ is the corresponding variation in atmospheric CO₂ concentration acquired from the Earth System Research Laboratory of NOAA⁸⁴ (<https://www.esrl.noaa.gov/gmd/ccgg/trends/>). The analysis was complemented by the estimation of the combined direct and indirect effect of eCO₂ on GPP quantified as:

$$\text{eCO}_2(\text{net})_{\text{obs}} = \frac{\Delta\text{GPP}_{\text{obs}}}{\Delta\text{CO}_2} \quad (8)$$

where $\Delta\text{GPP}_{\text{obs}}$ and ΔCO_2 represent the change in the mean growing-season GPP_{obs} and CO₂ concentration, respectively, computed between the two sub-periods. We finally derived the observed indirect effect of eCO₂ on vegetation photosynthesis via associated climate change in a given period by combining Eq. (7) and Eq. (8) as follows:

$$\text{eCO}_2(\text{ind})_{\text{obs}} = \frac{\Delta\text{GPP}_{\text{obs}}}{\Delta\text{CO}_2} - \frac{\Delta\text{GPP}_{\text{obs}}^{\text{CA}}}{\Delta\text{CO}_2^{\text{CA}}} \quad (9)$$

The approach assumes that both direct and indirect eCO_2 effects on GPP are annual and do not have legacy effects, and that eCO_2 is the dominant factor of climate change in the short-term. The above-described analyses were carried out at the grid-cell scale and separately for the periods 1982–1996 and 2000–2014. Changes between the two periods were then used to quantify the historical variations in the indirect effect of eCO_2 from observations (Fig. 1e, f).

To further test the robustness of our methods, a set of additional experiments were produced. First, the observed direct effect of eCO_2 was estimated using an alternative approach based on multiple non-linear regression model (i.e., Eq. (4)) in combination with CRU v4.05 climate dataset and GPP_{obs} . The obtained results, expressed as $eCO_2(dir)_{obs-RM}$, were confronted with climate analog-derived $eCO_2(dir)_{obs}$ estimates (i.e., obs-RM and obs in Fig. 3a). Second, the climate analog approach presented above and applied to observations was also implemented with CMIP6 model outputs in fully-coupled experiments to verify the consistency with results obtained from factorial simulations described in Eq. (3) (Supplementary Fig. 28).

Statistical analysis

To explore the dynamics of the indirect effect of eCO_2 on vegetation carbon uptake during the historical period, we quantified the temporal changes in model-based $eCO_2(ind)$ and observation-based $eCO_2(ind)_{obs}$ retrieved for the two independent periods 1982–1996 and 2000–2014. The significance of the emerging changes was assessed through t test. Results presented in the main text refer to analyses conducted over 15-year time windows. Results obtained for different temporal window lengths (12 and 16 years) are quantified as well to verify the robustness of our results (Fig. 1a and Supplementary Fig. 1).

In exploring the projected changes in $eCO_2(ind)$ from CMIP6 model simulations, we refer to six 15-year consecutive and independent periods, namely 2011–2025, 2026–2040, 2041–2055, 2056–2070, 2071–2085, 2086–2100 (Fig. 2a). We considered a series of not overlapped temporal windows to eliminate the possible impact of autocorrelation. To better disentangle the signal of future variation in $eCO_2(ind)$, we compared the $eCO_2(ind)$ during the last 15 years (2086–2100) against that one originating from the first 15 years of the historical period investigated here (1982–1996) and assessed the statistical significance of the change through t test.

Furthermore, to properly represent the generality of the relationships between the direction and extent of changes in $eCO_2(ind)$ and local aridity conditions, we performed binned average analysis across environmental gradients. Such spatial averaging minimizes the uncertainty originating from spatial heterogeneity (e.g., the difference in topography and vegetation type) that may randomly affect the control of climate change on vegetation carbon uptake (Figs. 1d and 4c, d).

Data availability

All datasets used in this study are publicly available as referenced in Methods. Source data are provided with this paper.

Code availability

The custom MATLAB (R2023a) codes written to read and analyze data and generated figures are publicly available at <https://doi.org/10.5281/zenodo.10451254>.

References

- Ahlström, A. et al. The dominant role of semi-arid ecosystems in the trend and variability of the land CO_2 sink. *Science* **348**, 895–899 (2015).
- Friedlingstein, P. et al. Global carbon budget 2022. *Earth Syst. Sci. Data* **14**, 4811–4900 (2022).
- Ballantyne, A., Alden, C., Miller, J., Tans, P. & White, J. Increase in observed net carbon dioxide uptake by land and oceans during the past 50 years. *Nature* **488**, 70–72 (2012).
- Schimel, D., Stephens, B. & Fisher, J. Effect of increasing CO_2 on the terrestrial carbon cycle. *Proc. Natl Acad. Sci. USA* **112**, 436–441 (2015).
- Keenan, T. et al. Recent pause in the growth rate of atmospheric CO_2 due to enhanced terrestrial carbon uptake. *Nat. Commun.* **7**, 13428 (2016).
- Liu, Y. et al. Field-experiment constraints on the enhancement of the terrestrial carbon sink by CO_2 fertilization. *Nat. Geosci.* **12**, 809–814 (2019).
- Jiang, M. et al. The fate of carbon in a mature forest under carbon dioxide enrichment. *Nature* **580**, 227–231 (2020).
- Smith, W. et al. Large divergence of satellite and Earth system model estimates of global terrestrial CO_2 fertilization. *Nat. Clim. Change* **6**, 306–310 (2016).
- Wang, S. et al. Recent global decline of CO_2 fertilization effects on vegetation photosynthesis. *Science* **370**, 1295–1300 (2020).
- Zhu, P. et al. Elevated atmospheric CO_2 negatively impacts photosynthesis through radiative forcing and physiology-mediated climate feedback. *Geophys. Res. Lett.* **44**, 1956–1963 (2017).
- Green, J. et al. Large influence of soil moisture on long-term terrestrial carbon uptake. *Nature* **565**, 476–479 (2019).
- Duffy, K. et al. How close are we to the temperature tipping point of the terrestrial biosphere? *Sci. Adv.* **7**, eaay1052 (2021).
- Peñuelas, J. et al. Shifting from a fertilization-dominated to a warming-dominated period. *Nat. Ecol. Evol.* **1**, 1438–1445 (2017).
- Cheng, L. et al. Recent increases in terrestrial carbon uptake at little cost to the water cycle. *Nat. Commun.* **8**, 110 (2017).
- Mitchard, E. The tropical forest carbon cycle and climate change. *Nature* **559**, 527–534 (2018).
- Bala, G. et al. An estimate of equilibrium sensitivity of global terrestrial carbon cycle using NCAR CCSM4. *Clim. Dyn.* **40**, 1671–1686 (2013).
- Gedalof, Z. & Berg, A. Tree ring evidence for limited direct CO_2 fertilization of forests over the 20th century. *Glob. Biogeochem. Cycles* **24**, GB3027 (2010).
- Reich, P., Hobbie, S. & Lee, T. Plant growth enhancement by elevated CO_2 eliminated by joint water and nitrogen limitation. *Nat. Geosci.* **7**, 920–924 (2014).
- Yuan, W. et al. Increased atmospheric vapor pressure deficit reduces global vegetation growth. *Sci. Adv.* **5**, eaax1396 (2019).
- Hickler, T. et al. CO_2 fertilization in temperate FACE experiments not representative of boreal and tropical forests. *Glob. Change Biol.* **14**, 1531–1542 (2008).
- Wang, T. et al. Emerging negative impact of warming on summer carbon uptake in northern ecosystems. *Nat. Commun.* **9**, 5391 (2018).
- Piao, S. et al. Evidence for a weakening relationship between interannual temperature variability and northern vegetation activity. *Nat. Commun.* **5**, 5018 (2014).
- Ding, J. et al. Increasingly important role of atmospheric aridity on Tibetan alpine grasslands. *Geophys. Res. Lett.* **45**, 2852–2859 (2018).
- Gonsamo, A. et al. Greening drylands despite warming consistent with carbon dioxide fertilization effect. *Glob. Change Biol.* **27**, 3336–3349 (2021).
- Jiao, W. et al. Observed increasing water constraint on vegetation growth over the last three decades. *Nat. Commun.* **12**, 3777 (2021).
- Xu, C. et al. Increasing impacts of extreme droughts on vegetation productivity under climate change. *Nat. Clim. Change* **9**, 948–953 (2019).

27. Seddon, A., Macias-Fauria, M., Long, P., Benz, D. & Willis, K. Sensitivity of global terrestrial ecosystems to climate variability. *Nature* **531**, 229–232 (2016).
28. Fu, Z. et al. Atmospheric dryness reduces photosynthesis along a large range of soil water deficits. *Nat. Commun.* **13**, 989 (2022).
29. Eyring, V. et al. Overview of the Coupled Model Intercomparison Project Phase 6 (CMIP6) experimental design and organization. *Geosci. Model Dev.* **9**, 1937–1958 (2016).
30. Jones, C. et al. C4MIP – the coupled climate–carbon cycle model intercomparison project: experimental protocol for CMIP6. *Geosci. Model Dev.* **9**, 2853–2880 (2016).
31. Zhang, Y., Song, C., Band, L. & Sun, G. No proportional increase of terrestrial gross carbon sequestration from the greening Earth. *J. Geophys. Res. Atmos.* **124**, 2540–2553 (2019).
32. Badgley, G., Field, C. & Berry, J. Canopy near-infrared reflectance and terrestrial photosynthesis. *Sci. Adv.* **3**, e1602244 (2017).
33. Mahony, C., Cannon, A., Wang, T. & Aitken, S. A closer look at novel climates: new methods and insights at continental to landscape scales. *Glob. Change Biol.* **23**, 3934–3955 (2017).
34. Friedlingstein, P. et al. Climate–carbon cycle feedback analysis: results from the C⁴MIP model intercomparison. *J. Clim.* **19**, 3337–3353 (2006).
35. Ciais, P. et al. Five decades of northern land carbon uptake revealed by the interhemispheric CO₂ gradient. *Nature* **568**, 221–225 (2019).
36. Pan, Y. et al. A large and persistent carbon sink in the world's forests. *Science* **333**, 988–993 (2011).
37. Sitch, S. et al. Recent trends and drivers of regional sources and sinks of carbon dioxide. *Biogeosciences* **12**, 653–679 (2015).
38. Dai, A. Increasing drought under global warming in observations and models. *Nat. Clim. Change* **3**, 52–58 (2013).
39. Berg, A., Sheffield, J. & Milly, P. Divergent surface and total soil moisture projections under global warming. *Geophys. Res. Lett.* **44**, 236–244 (2017).
40. Cook, B. et al. Twenty-first century drought projections in the CMIP6 forcing scenarios. *Earth's Future* **8**, e2019EF001461 (2020).
41. United Nations Environment Program. World Atlas of Desertification. 182 (1997).
42. Ukkola, A. et al. Reduced streamflow in water-stressed climates consistent with CO₂ effects on vegetation. *Nat. Clim. Change* **6**, 75–78 (2016).
43. Peters, W. et al. Increased water-use efficiency and reduced CO₂ uptake by plants during droughts at a continental scale. *Nat. Geosci.* **11**, 744–748 (2018).
44. Piao, S. et al. Characteristics, drivers and feedbacks of global greening. *Nat. Rev. Earth Environ.* **1**, 14–27 (2020).
45. Kannenberg, S., Driscoll, A., Szejner, P., Anderegg, W. & Ehleringer, J. Rapid increases in shrubland and forest intrinsic water-use efficiency during an ongoing megadrought. *Proc. Natl. Acad. Sci. USA* **118**(52), e2118052118 (2021).
46. Arora, V. et al. Carbon–concentration and carbon–climate feedbacks in CMIP6 models and their comparison to CMIP5 models. *Biogeosciences* **17**, 4173–4222 (2020).
47. Nemani, R. et al. Climate-driven increases in global terrestrial net primary production from 1982 to 1999. *Science* **300**, 1560–1563 (2003).
48. Li, W. et al. Widespread increasing vegetation sensitivity to soil moisture. *Nat. Commun.* **13**, 3959 (2022).
49. Buermann, W. et al. Widespread seasonal compensation effects of spring warming on northern plant productivity. *Nature* **562**, 110–114 (2018).
50. Pearson, R. et al. Shifts in Arctic vegetation and associated feedbacks under climate change. *Nat. Clim. Change* **3**, 673–677 (2013).
51. Myers-Smith, I. et al. Complexity revealed in the greening of the Arctic. *Nat. Clim. Change* **10**, 106–117 (2020).
52. Forzieri, G., Dakos, V., McDowell, N., Ramdane, A. & Cescatti, A. Emerging signals of declining forest resilience under climate change. *Nature* **608**, 534–539 (2022).
53. Adams, M., Buckley, T., Binkley, D., Neumann, M. & Turnbull, T. CO₂, nitrogen deposition and a discontinuous climate response drive water use efficiency in global forests. *Nat. Commun.* **12**, 5194 (2021).
54. Seidl, R. et al. Forest disturbances under climate change. *Nat. Clim. Change* **7**, 395–402 (2017).
55. Forzieri, G. et al. Emergent vulnerability to climate-driven disturbances in European forests. *Nat. Commun.* **12**, 1081 (2021).
56. Anderegg, W. et al. Tree mortality from drought, insects, and their interactions in a changing climate. *New Phytol.* **208**, 674–683 (2015).
57. Bonan, G. & Doney, S. Climate, ecosystems, and planetary futures: the challenge to predict life in Earth system models. *Science* **359**, eaam8328 (2018).
58. McDowell, N. et al. Pervasive shifts in forest dynamics in a changing world. *Science* **368**, eaaz9463 (2020).
59. Senf, C. & Seidl, R. Mapping the forest disturbance regimes of Europe. *Nat. Sustain.* **4**, 63–70 (2021).
60. D'Orangeville, L. et al. Beneficial effects of climate warming on boreal tree growth may be transitory. *Nat. Commun.* **9**, 3213 (2018).
61. Reichstein, M. et al. Climate extremes and the carbon cycle. *Nature* **500**, 287–295 (2013).
62. Frank, D. et al. Effects of climate extremes on the terrestrial carbon cycle: concepts, processes and potential future impacts. *Glob. Change Biol.* **21**, 2861–2880 (2015).
63. Obermeier, W. et al. Reduced CO₂ fertilization effect in temperate C3 grasslands under more extreme weather conditions. *Nat. Clim. Change* **7**, 137–141 (2017).
64. Meinshausen, M. et al. The shared socio-economic pathway (SSP) greenhouse gas concentrations and their extensions to 2500. *Geosci. Model Dev.* **13**, 3571–3605 (2020).
65. Gillett, N. et al. The detection and attribution model inter-comparison project (DAMIP v1.0) contribution to CMIP6. *Geosci. Model Dev.* **9**, 3685–3697 (2016).
66. Spafford, L. & MacDougall, A. Validation of terrestrial biogeochemistry in CMIP6 Earth system models: a review. *Geosci. Model Dev.* **14**, 5863–5889 (2021).
67. Novick, K. et al. The increasing importance of atmospheric demand for ecosystem water and carbon fluxes. *Nat. Clim. Change* **6**, 1023–1027 (2016).
68. Abbott, P. & Tabony, R. The estimation of humidity parameters. *Meteorol. Mag.* **114**, 49–56 (1985).
69. Allen, R. G., Pereira, L. S., Raes, D. & Smith, M. Crop evapotranspiration-guidelines for computing crop water requirements. FAO irrigation and drainage paper no. 56 (1998).
70. Cook, K. & Vizy, E. Impact of climate change on mid-twenty-first century growing seasons in Africa. *Clim. Dyn.* **39**, 2937–2955 (2012).
71. Wang, S. & Zhang, Y. Long-term (1982–2018) global gross primary production dataset based on NIRv [Data set]. <https://doi.org/10.6084/m9.figshare.12981977.v2> (2020).
72. Wang, S., Zhang, Y., Ju, W., Qiu, B. & Zhang, Z. Tracking the seasonal and inter-annual variations of global gross primary production during last four decades using satellite near-infrared reflectance data. *Sci. Total Environ.* **755**, 142569 (2021).
73. Harris, I., Osborn, T., Jones, P. & Lister, D. Version 4 of the CRU TS monthly high-resolution gridded multivariate climate dataset. *Sci. Data* **7**, 109 (2020).
74. European Space Agency (ESA). Land Cover CCI Product User Guide Version 2 (2017).
75. Skinner, C., Poulsen, C. & Mankin, J. Amplification of heat extremes by plant CO₂ physiological forcing. *Nat. Commun.* **9**, 1094 (2018).
76. Park, S., Kim, J. & Kug, J. The intensification of Arctic warming as a result of CO₂ physiological forcing. *Nat. Commun.* **11**, 2098 (2020).

77. Meinshausen, M. et al. Historical greenhouse gas concentrations for climate modelling (CMIP6). *Geosci. Model. Dev.* **10**, 2057–2116 (2017).
78. Zhang, X. et al. Linear and nonlinear effects of dominant drivers on the trends in global and regional land carbon uptake: 1959 to 2013. *Geophys. Res. Lett.* **43**, 1607–1614 (2016).
79. Felton, A., Knapp, A. & Smith, M. Precipitation–productivity relationships and the duration of precipitation anomalies: an underappreciated dimension of climate change. *Glob. Change Biol.* **27**, 1127–1140 (2021).
80. Chen, Z., Wang, W., Cescatti, A. & Forzieri, G. Climate-driven vegetation greening further reduces water availability in drylands. *Glob. Change Biol.* **29**, 1421–1679 (2023).
81. Fitzpatrick, M. & Dunn, R. Contemporary climatic analogs for 540 North American urban areas in the late 21st century. *Nat. Commun.* **10**, 614 (2019).
82. Williams, J., Jackson, S. & Kutzbach, J. Projected distributions of novel and disappearing climates by 2100 AD. *Proc. Natl Acad. Sci. USA* **104**, 5738–5742 (2007).
83. Ordóñez, A. & Williams, J. Projected climate reshuffling based on multivariate climate-availability, climate-analog, and climate-velocity analyses: implications for community disaggregation. *Clim. Change* **119**, 659–675 (2013).
84. Masarie, K. & Tans, P. Extension and integration of atmospheric carbon dioxide data into a globally consistent measurement record. *J. Geophys. Res. Atmos.* **100**, 11593–11610 (1995).

Acknowledgements

W.W. was supported by the National Natural Science Foundation of China (grant no. U2240218). G.F. was supported by the Horizon Europe Project ECO2ADAPT (grant no. 101059498).

Author contributions

W.W. and Z.C. conceived and designed the research; Z.C. implemented the data analysis; G.F. and A.C. contributed analysis ideas; Z.C. interpreted the results and drafted the initial manuscript; W.W., G.F., and A.C. provided suggestions and further improved writing. All authors approved the final version of this manuscript.

Competing interests

The authors declare no competing interests.

Additional information

Supplementary information The online version contains supplementary material available at <https://doi.org/10.1038/s41467-024-45957-x>.

Correspondence and requests for materials should be addressed to Weiguang Wang.

Peer review information : *Nature Communications* thanks the anonymous reviewers for their contribution to the peer review of this work. A peer review file is available.

Reprints and permissions information is available at <http://www.nature.com/reprints>

Publisher's note Springer Nature remains neutral with regard to jurisdictional claims in published maps and institutional affiliations.

Open Access This article is licensed under a Creative Commons Attribution 4.0 International License, which permits use, sharing, adaptation, distribution and reproduction in any medium or format, as long as you give appropriate credit to the original author(s) and the source, provide a link to the Creative Commons licence, and indicate if changes were made. The images or other third party material in this article are included in the article's Creative Commons licence, unless indicated otherwise in a credit line to the material. If material is not included in the article's Creative Commons licence and your intended use is not permitted by statutory regulation or exceeds the permitted use, you will need to obtain permission directly from the copyright holder. To view a copy of this licence, visit <http://creativecommons.org/licenses/by/4.0/>.

© The Author(s) 2024